JACS
JOURNAL OF THE AMERICAN CHEMICAL SOCIETY
pubs.acs.org/JACS
Article

DNA-Origami Line-Actants Control Domain Organization and Fission in Synthetic Membranes

Roger Rubio-Sánchez,* Bortolo Matteo Mognetti, Pietro Cicuta, and Lorenzo Di Michele*

Cite This: J. Am. Chem. Soc. 2023, 145, 11265−11275
Read Online
ACCESS | Metrics & More | Article Recommendations | Supporting Information

ABSTRACT: Cells can precisely program the shape and lateral organization of their membranes using protein machinery. Aiming to replicate a comparable degree of control, here we introduce DNA-origami line-actants (DOLAs) as synthetic analogues of membrane-sculpting proteins. DOLAs are designed to selectively accumulate at the line-interface between coexisting domains in phase-separated lipid membranes, modulating the tendency of the domains to coalesce. With experiments and coarse-grained simulations, we demonstrate that DOLAs can reversibly stabilize two-dimensional analogues of Pickering emulsions on synthetic giant liposomes, enabling dynamic programming of membrane lateral organization. The control afforded over membrane structure by DOLAs extends to three-dimensional morphology, as exemplified by a proof-of-concept synthetic pathway leading to vesicle fission. With DOLAs we lay the foundations for mimicking, in synthetic systems, some of the critical membrane-hosted functionalities of biological cells, including signaling, trafficking, sensing, and division.

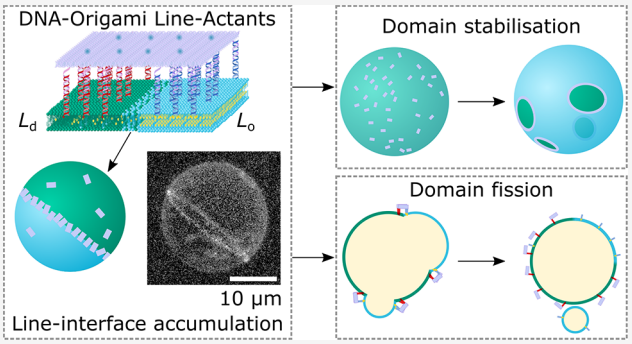

INTRODUCTION

Biological membranes coordinate numerous pathways critical to life, from trafficking to signal transduction and cellular motility,[1] many of which rely on regulating the distribution and interactions of membrane machinery. Among other regulatory principles, cells are believed to exploit membrane phase separation and critical composition fluctuations to dynamically generate local heterogeneity.[2−10] Cell membranes are also known to contain inclusions that can accumulate at the line-interface between coexisting lipid domains[11−15] and relax the associated line tension.[16−18] It has been proposed that cells use these *line-actants* as an additional means to dynamically control membrane phase behavior and the lateral organization of membrane inclusions[19] underpinning, for instance, the function of signaling hubs[20,21] and the generation of endo/exosomes.[22,23]

Artificial cell science aims to construct, from the bottom up, synthetic analogues of biological cells that mimic their sophisticated behaviors[24,25] and are expected to widely impact next-generation diagnostics, therapeutics, and bioprocessing.[26−28] Often constructed from lipid bilayers,[29] synthetic-cell membranes have been engineered to replicate an array of biomimetic responses,[30] including mechanotransduction,[31] energy conversion,[32−34] and membrane deformation.[35]

In parallel to solutions relying on reconstituted membrane proteins,[32−34] fully synthetic DNA nanodevices,[36] anchored to the bilayers by means of hydrophobic tags, have emerged as a versatile toolkit for biomembrane engineering,[37−39] having enabled the design of biomimetic pathways for transport,[40−43] trafficking,[44,45] cell adhesion,[46,47] tissue formation,[48−50] signal detection,[51] membrane remodeling,[52−55] and surface patterning.[56−59]

Despite these advances, the design of pathways enabling systematic control over the local structure and composition of synthetic-cell membranes, to the same degree of what is afforded by extant biological machinery, remains an elusive task.

Here we introduce DNA-origami line-actants (DOLAs) to control the formation, stability, and three-dimensional morphology of lipid domains on synthetic bilayers. Leveraging the modularity of amphiphilic DNA nanotechnology,[56] we designed DOLAs to selectively accumulate at the line-interface between coexisting domains on giant unilamellar vesicles (GUVs). Using a combination of experiments and coarse-grained simulations, we show that, similar to interfacial inclusions in three dimensions, DOLAs modulate the tendency of lipid domains to coalesce, stabilizing two-dimensional analogues of Pickering emulsions. The devices can be deactivated upon exposure to a molecular stimulus, triggering domain coarsening and unlocking the sought dynamic control

Received: February 12, 2023
Published: May 10, 2023

https://doi.org/10.1021/jacs.3c01493
J. Am. Chem. Soc. 2023, 145, 11265−11275

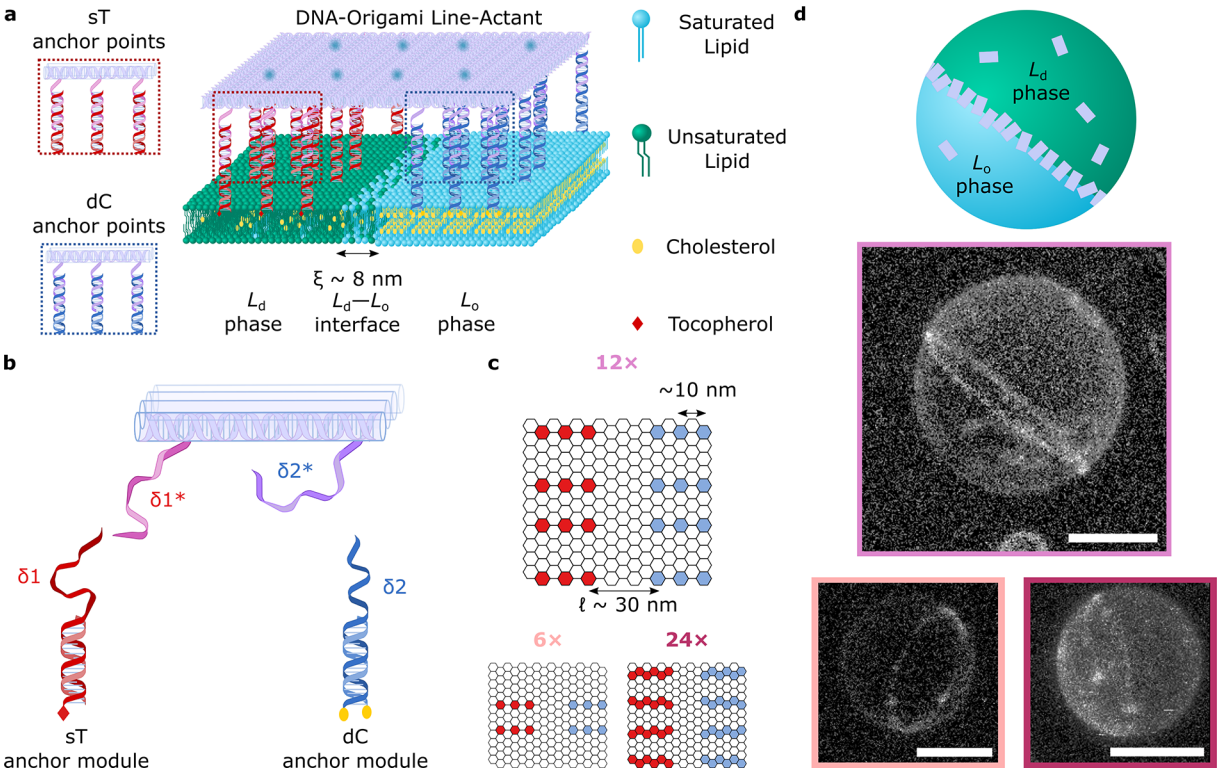

Figure 1. DNA-origami line-active agents enrich the line-interface of phase-separated GUVs. (a) Schematic representation of a multicomponent lipid bilayer membrane composed of saturated and unsaturated lipids mixed with sterols, displaying liquid-ordered (L_o) and liquid-disordered (L_d) phase coexistence. The outer leaflet of the membrane is decorated with a DNA-origami line-actant (DOLA), where amphiphilic anchor modules bearing single-tocopherol (sT) and double-cholesterol (dC) motifs enrich their preferred (L_d and L_o, respectively) phases, driving accumulation of the DOLA at the L_d–L_o interface. (b) Selected staples on the origami (see Supplementary Table 2) were extended to include overhang domains $\delta1^*$ and $\delta2^*$, with complementarity to dC (blue) or sT (red) anchor modules, respectively (Supplementary Tables 3 and 4). Note that tiles are expected to have all of their $\delta1$ and $\delta2$ overhangs saturated with sT and dC anchoring modules, owing to the strong affinity between overhangs (see Supplementary Note III). We also expect partially bound states, in which tiles are linked to the membrane through a subset of the available anchors, to be thermodynamically unlikely. (c) Hexagonal grids depict the arrangement of staples across the origami plates, where each hexagon corresponds to the 3′ terminus of a staple. We positioned sets of 6× (light pink), 12× (pink), or 24× (magenta) overhangs targeting the same type of anchor-points. The two sets of anchors are separated by a distance l ~ 30nm (6× and 12×) or l ~ 25nm (24×). (d) (Top) Schematic representation a demixed GUV where the L_d–L_o interface is enriched with DOLAs. (Bottom) Representative 3D views of phase-separated vesicles with a Janus-like morphology showing line-accumulation of fluorescent (Alexa488) 6× (light pink), 12× (pink), or 24× (magenta) DOLAs, as reconstructed from a confocal z-stack using Volume Viewer (FIJI[60]) with contrast enhancement (see Supplementary Figure 3 for reconstructions without contrast enhancement and confocal equatorial cross sections highlighting line-accumulation). Scale bars = 10 μm.

over lateral membrane organization. Combined with osmotic unbalance, we demonstrate DOLAs can form the basis of a synthetic pathway leading to membrane budding-off and fission, exemplifying three-dimensional morphological control.

Owing to their modular design and robust working principle, we argue that DOLAs could constitute a versatile toolkit for synthetic-cell membrane engineering, allowing us to take full advantage of the rich phenomenology of lipid phase separation and design ever-more-advanced membrane-hosted functionalities.

RESULTS AND DISCUSSION

Engineering Line-Actants with DNA Nanostructures. Our design of choice for DNA line-actants, depicted schematically in Figure 1a, exploits the versatility of the Rothemund rectangular origami (RRO) as a "molecular breadboard", with an array of regularly spaced binding sites.[61−64] The rectangular tiles (Supplementary Figure 1 and Supplementary Table 1) feature two sets of either 6, 12, or 24 single-stranded (ss) DNA overhangs extended from the same face of the origami, as shown in Figure 1b. The sticky ends, with sequence $\delta1^*$ or $\delta2^*$, can respectively bind complementary overhangs on double-stranded (ds) DNA *anchoring modules* functionalized with two cholesterol moieties (dC) or a single tocopherol (sT).[56] We have recently determined that dC and sT modules display, respectively, thermodynamic preferences for accumulating within liquid-ordered (L_o) and liquid-disordered (L_d) domains of phase-separated membranes. Specifically, transporting a dC module from L_d to L_o produces a moderately favorable free-energy shift ($\Delta G^{dC}_{p,L_o}$) of ~−0.8 k_BT, while sT has a stronger affinity for disordered domains ($\Delta G^{sT}_{p,L_o} \approx 1.9\ k_BT$).[56] The two sets of dC and sT modules were distributed on opposite halves of the tiles, with a spacing of l ~ 25−30nm between the two distinct sets of anchors (Figure 1b). Because l is comfortably greater than the estimated width of the boundary separating L_o and L_d phases (ξ ~ 8 nm, Supplementary Note I), free-energy minimization is expected to drive the accumulation of the tiles across line-interfaces, accommodating each set of anchors in their respective preferred phase (Figure 1a). We produced three DOLA designs, with either 6×, 12×, or 24× anchors of each type,

https://doi.org/10.1021/jacs.3c01493
J. Am. Chem. Soc. 2023, 145, 11265−11275

expecting an increase in the free-energy gain associated with line-accumulation for a larger number of anchors (Figure 1c).

DOLAs were further labeled with fluorescent (Alexa488) beacons, located on the face opposite to that hosting the anchors (Supplementary Figure 2 and Supplementary Table 5), thus allowing us to monitor their distribution by means of confocal microscopy. Accumulation of the three DOLA designs at the L_d−L_o line-interface in phase-separated GUVs (DOPC/DPPC/Chol 2:2:1) is demonstrated in Figure 1d with confocal 3D reconstructions, where the equatorial boundary separating the two hemispherical domains is clearly delineated by the fluorescent plates.

A custom-built image segmentation routine, detailed in Supplementary Note II and Supplementary Figure 4, was applied to confocal data to sample the DOLAs' fluorescence-intensity profile across line-interfaces, as sketched in Figure 2a. The resulting curves, shown in Figure 2b, display clear peaks at the L_d−L_o boundary location ($x = 0$), confirming line-accumulation. As detailed in Supplementary Note II, fitting of the diffraction-limited fluorescent peak and baseline signals from the surrounding L_d and L_o regions allowed us to estimate a line-partitioning coefficient $K_{p,int}$, defined as the ratio between the surface density of origami at the line-interface and the average origami surface density on the entire GUV.

Figure 2c summarizes the experimentally determined $K_{p,int}$ for the three tested designs, rendering similar results for the 12× and 24× tiles, with a slightly larger value for the 6× variant. Line-interface adsorption models, outlined in Supplementary Note III (see associated Supplementary Figure 5 and Supplementary Tables 6, 7, and 8), enable the estimation of $K_{p,int}$ for the three DOLA designs. We fitted the theoretical estimates to experimentally determined $K_{p,int}$ values, using the overall surface coverage of the origami on the GUVs, σ, as a fitting parameter. The obtained estimates of $1.5 < \sigma^{12\times}_{theory} < 9.3\%$ and $2.9 < \sigma^{24\times}_{theory} < 14.4\%$ for 12× and 24×, respectively, are in good agreement with the nominal experimental surface coverage $\sigma_{exp} \sim 5\%$ (Supplementary Figure 6). For the 6× design, we estimated $\sigma^{6\times}_{theory} < 3.2\%$, slightly below the nominal experimental value and reflecting the larger observed $K_{p,int}$ and the smaller absolute fluorescence-intensity values (see Supplementary Note III and Supplementary Figure 7). A smaller than expected σ is likely the result of a decreased membrane affinity, consistent with the smaller number of anchor-points available for the 6× tiles. It should further be noted that RRO tiles are prone to bending in the direction orthogonal to that of the double helices,[65] possibly leading to thermal fluctuations in curvature while tiles are in the bulk. These fluctuations would be suppressed upon confining the tiles to the membrane, which would carry an entropic penalty to tile−membrane binding. It is natural to expect that anchoring overhangs may limit the amplitude of shape fluctuations in the bulk, implying that designs with a higher number of anchoring points, i.e., 24× and 12×, would be less affected by the confinement entropic penalty compared to the (arguably) more flexible 6× design. Possible differences in spontaneous (equilibrium) curvature of the tile designs[66] may also impact membrane−tile affinity.

Fitted line-adsorption models allowed us to estimate the fraction of the line-interface occupied by DOLAs, ϕ (defined in Supplementary Note III; see Supplementary Figure 5), summarized in Figure 2d. Expectedly, we note an increase in ϕ with increasing number of anchors, with the strongly binding 24× approaching saturation and the 6× leaving much of the line unoccupied, hence demonstrating control over the degree of line-accumulation by design. Note that the uncertainties in the estimate of the line-interface width ξ propagate to the values obtained for $K_{p,int}$ (see Supplementary Note III). As demonstrated in Supplementary Figure 8, however, relative trends with respect to tile design are robust, while changes to the values of ϕ are negligible.

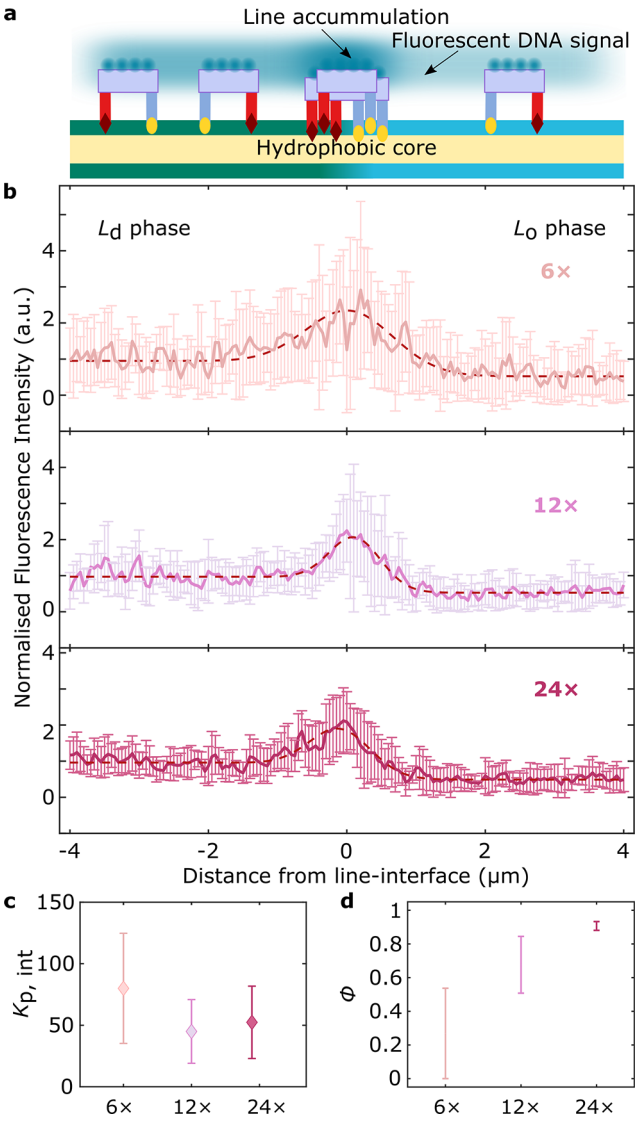

Figure 2. Line-accumulation of DOLAs is regulated by the number of anchors. (a) Schematic depiction of a demixed lipid membrane decorated with DOLAs, where fluorescent Alexa488 beacons enable the quantification of origami distribution from fluorescence intensity profiles (Supplementary Note II). (b) Line-interface accumulation conveyed as average fluorescence intensity ± standard deviation for line-interfaces decorated with 6×, 12×, or 24× DOLAs (sampled interfaces n = 12, 10, and 10, respectively). The profiles, as a function of distance from the line-interface ($x = 0$), have been normalized to the mean L_d-phase intensity. Red dashed lines are fits to eq S2 (Supplementary Note II), which models the experimental, diffraction-blurred, fluorescence intensity profile. (c) Line-partitioning coefficients ($K_{p,int}$) of DOLAs featuring sets of either 6×, 12×, or 24× dC/sT anchor-points. (d) Fraction of line-interface occupied (ϕ) by 6×, 12×, or 24× line-actants, computed using the experimental $K_{p,int}$ in our numerical line-adsorption model (see Supplementary Note III and Supplementary Figures 5, 6, 7, and 8).

https://doi.org/10.1021/jacs.3c01493
J. Am. Chem. Soc. 2023, 145, 11265−11275

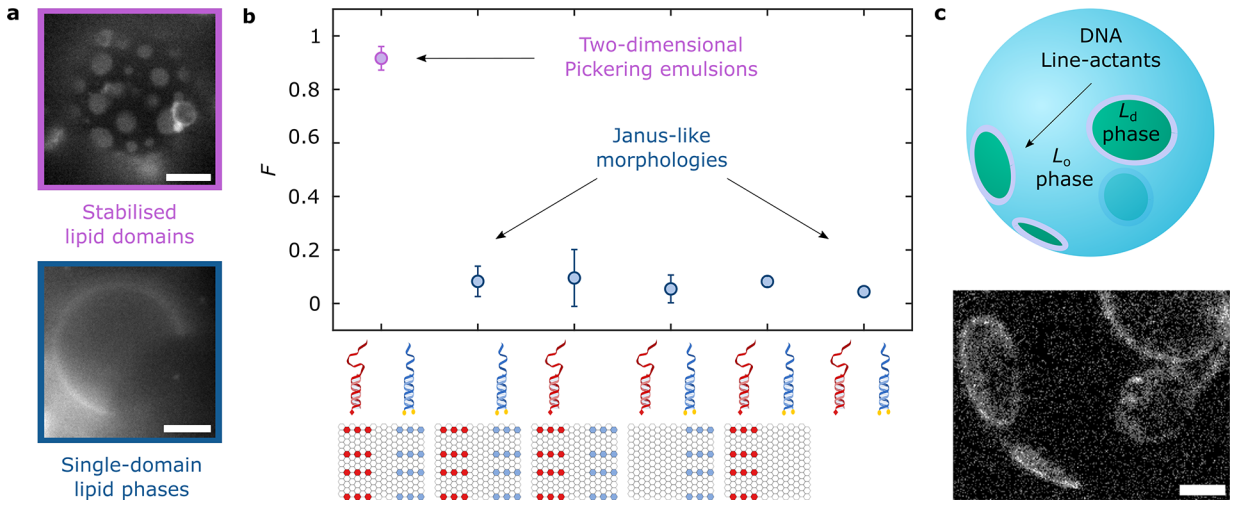

Figure 3. DOLAs stabilize two-dimensional analogues of Pickering emulsions. (a) Representative epifluorescence micrographs of demixed GUVs showing (top) stable lipid domains ∼3 h after phase separation in the presence of 12× DOLAs; (bottom) GUV lacking line-actants that equilibrated to produce a Janus morphology with two quasi-hemispherical L_d and L_o domains. Fluorescent marker is Texas Red-DHPE, which partitions to the L_d phase. (b) Programmable, domain-stabilizing, activity of DOLAs as conveyed by the fraction, F, of GUVs exhibiting more than two domains with respect to that of Janus vesicles. As shown in the graphical legend, besides the complete DOLAs (n = 363 GUVs), we exploited the modularity of the platform to produce various control functionalization schemes expected to lack line-active behavior, including omitting either sT (n = 97 GUVs) or dC (n = 187 GUVs) modules, using tiles that lack overhangs targeting sT (n = 125 GUVs) or dC (n = 165 GUVs), and omitting tiles altogether (n = 160 GUVs). (c) Line-accumulation of DOLAs scaffolds lipid domains and confers them with stability against coalescence, as shown with a 3D view of a reconstructed vesicle after heating above and quenching below the miscibility transition temperature. Interfacial accumulation of fluorescent (Alexa488) 12× DOLAs readily shows stable domains rendered from a representative confocal z-stack using Volume Viewer (FIJI[60]) with contrast enhancement (see Supplementary Figure 9 for reconstructions without contrast enhancement). All scale bars = 10 μm.

DOLAs Stabilize Two-Dimensional Pickering Emulsions. Having demonstrated that DOLAs can programmably accumulate at the boundary between coexisting lipid phases, we sought to verify whether accumulation leads to stabilization of the line-interface, as hypothesized for biological line-actants.[14] To this end, we decorated the phase-separating GUVs with 12× DOLAs at a nominal surface coverage of ∼30%, further promoting line-interface saturation ($\phi \sim 0.75-0.87$). The GUVs, fluorescently labeled with L_d-partitioning TexasRed-DHPE for ease of visualization, were heated to ∼37 °C, well above their miscibility transition temperature of $T_m \sim 33 \pm 1$ °C,[68] to induce lipid mixing. After incubating at high temperature for ∼5 min, the sample was quenched back to room temperature (T = 25 °C), leading to the nucleation of L_o or L_d domains in a background of the opposite phase.

In nonfunctionalized GUVs, domains rapidly coarsen until most vesicles display two quasi-hemispherical domains, resulting in Janus-like morphologies (Figure 3a, bottom). However, in DOLA-functionalized GUVs, coalescence was arrested, leading to morphologies with a large number of small, stable domains, analogous to two-dimensional Pickering emulsions (Figure 3a, top). To quantify the domain-stabilizing ability of DOLAs, we analyzed epifluorescence micrographs collected ∼3 h after quenching and extracted the fraction F of non-Janus vesicles, namely, those that failed to relax into the two-domain morphology. Results, summarized in Figure 3b, clearly demonstrate how most line-actant-decorated GUVs display Pickering morphologies (Figure 3a, top). In turn, the Janus morphology dominates when GUVs lack either dC or sT anchor modules, no tiles are included, or if the origami are prepared omitting the overhangs to target either dC or sT. The latter controls confirm that domain stabilization emerges solely thanks to line-interface accumulation of the rationally designed DOLAs, rather than as a result of nonspecific effects associated with the individual membrane inclusions.

As further confirmation that domain stabilization is underpinned by interfacial accumulation of the origami, vesicles lacking TexasRed-lipids and decorated with fluorescent DOLAs were subjected to an analogous heating−cooling program and inspected with confocal microscopy. Besides detecting domain stabilization, line-accumulation was confirmed at the boundaries of the stabilized lipid domains, as demonstrated in Figure 3c with a 3D confocal reconstruction.

Coarse-Grained Simulations Capture DOLA Line-Accumulation and Domain Stabilization. To further validate our line-actant engineering strategy, we conducted Monte Carlo (MC) simulations using a coarse-grained representation of the experimental system. As presented in Figure 4a and detailed in Supplementary Note IV, we defined a two-dimensional Ising model on a triangular lattice, which displays phase coexistence at sufficiently low temperature. We interpret the phase rich in spin s = 1 (green) as L_d and that rich in s = −1 (blue) as L_o. Rectangular tiles were included with anchor-points arranged on the lattice according to their nominal position on the DOLAs. Interaction free energies between dC/sT anchors and their lipid microenvironment were modeled in the system's Hamiltonian as $J_{dC}\cdot\tilde{s}$ and $J_{sT}\cdot\tilde{s}$, respectively, where $\tilde{s}$ is the sum of the spins over the lattice site hosting the anchor and its six nearest neighbors ($\tilde{s} \in [-7, -5, ..., 5, 7]$). The anchor-coupling constant values were chosen as J_{sT} = 0.136 k_BT and J_{dC} = −0.057 k_BT, reflecting the experimentally determined partitioning free energies of the modules (see Supplementary Note IV and ref 56).

To replicate the experimental protocol, we prepared high-temperature systems with uniform spin (and tile) distributions, before quenching to a lower temperature at which demixing

https://doi.org/10.1021/jacs.3c01493
J. Am. Chem. Soc. 2023, 145, 11265−11275

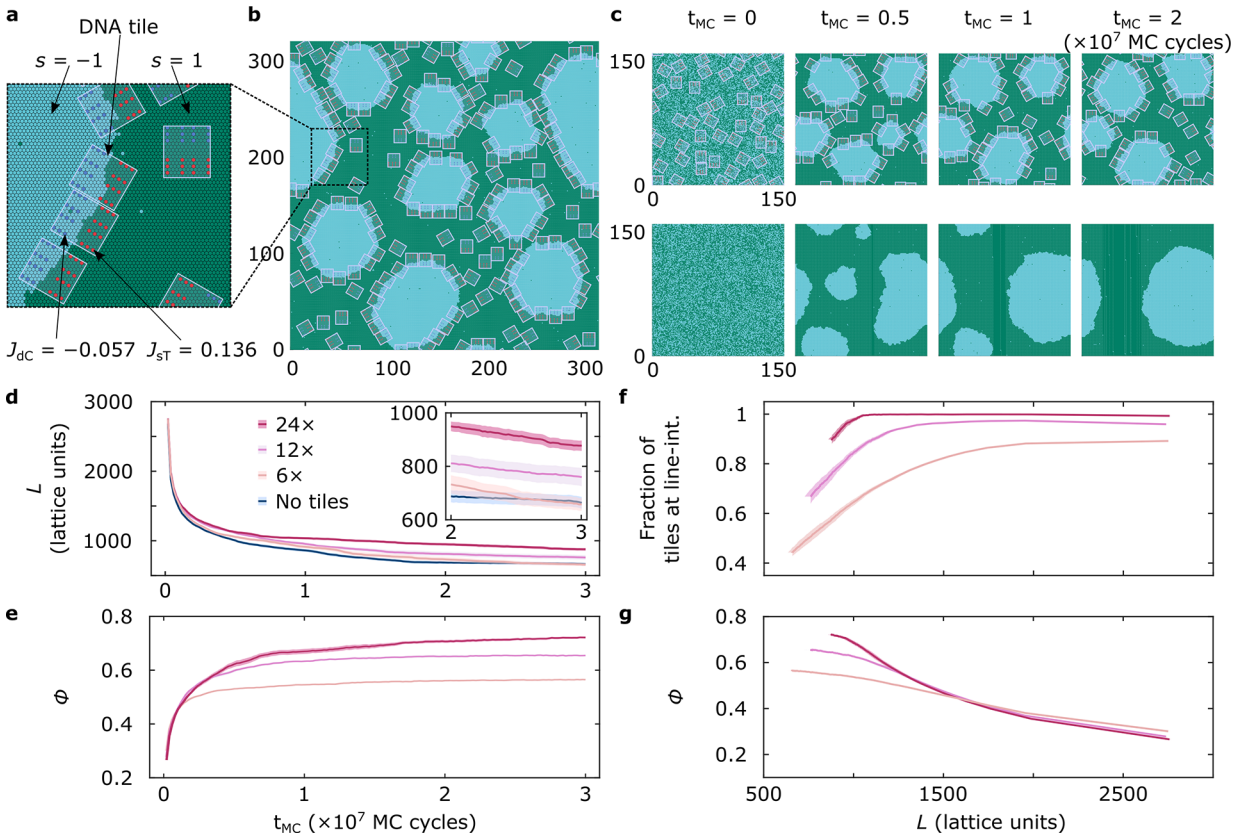

Figure 4. Coarse-grained simulations replicate DOLA line-accumulation and domain stabilization. (a) Representation of the developed Ising model with hexagonal unit cells carrying spins of $s = 1$ (green) and $s = -1$ (blue). Neighboring spins interact through a coupling parameter $J = 0.55\ k_BT$, chosen to roughly replicate the expected experimental line tension ∼1 pN.[67] Anchor points on the tiles are arranged based on the 12× DOLA design. Each anchor is located at an Ising lattice point and contributes with a free-energy term $J_x \sum_{i=1}^{7} s_i$, where s_i indicates the spins of the lattice point hosting the anchor and the 6 nearest neighbors, and J_x is a coupling constant taking different values for sT ($J_{sT} = 0.136\ k_BT$) and dC ($J_{dC} = -0.057\ k_BT$) to account for the different partitioning tendencies. (b) Representative snapshot of a simulation trajectory after $t_{MC} = 2$ (×10^7 MC cycles), where tiles stabilize blue domains by accumulating at their boundary. Box size: 320 × 372 lattice points. (c) Snapshots exemplifying the time-evolution of representative simulations, one including 12× DOLAs, where multiple domains retain stability even after $t_{MC} = 2 \times 10^7$ MC cycles (top), and the second lacking tiles and equilibrating to form a single domain (bottom). Box size: 160 × 172 lattice points. (d) Time dependence of the overall length of the line-interface (L) in simulations containing the three tested DOLA designs or no tiles, quantifying DOLA-induced interface stabilization. (e) Line-accumulation of 6×, 12×, and 24× DOLAs conveyed by the time-evolution of the fraction of line-interface (ϕ) occupied by tiles. A tile is said to be at the line when featuring at least 80% of favorable anchor−spin interactions relative to the total contacts (Supplementary Figure 12). (f) Fraction of the tiles present in the system located at the interface, showing that designs remain pinned at the line more readily as the latter shrinks. (g) Fraction of the line-interface (ϕ) occupied by tiles as a function of line length (L). The monotonic decrease is sharper for stronger-binding tiles. Panels d−g show mean (solid line) ± standard error of the mean (shaded regions) computed from $n = 15$ independent simulation trajectories. When errors are not visible, their values are smaller than the thickness of the solid line.

occurs. The quenching temperature was chosen to replicate the experimental line tension of ∼1 pN[67] (see Supplementary Note IV). The system was simulated with Kawasaki dynamics,[69] conserving the number of $s = -1$ and $s = 1$ spins, initially set to a ratio of 2/3. The tiles, present at a surface coverage $\sigma = 30\%$, readily localized at the boundaries of the blue domains emerging after quenching, leading to their stabilization (see Figure 4b and Supplementary Movie 1). Figure 4c compares the time-evolution of systems featuring and lacking 12× tiles. When tiles were present, coarsening was slowed down and small domains persisted at long simulation times ($t_{MC} = 2 \times 10^7$ steps). Conversely, over the same time window, the system lacking the tiles achieved complete coarsening, resulting in a morphology with one domain of each phase, analogous to the Janus GUVs (Supplementary Movies 2 and 3, respectively). Supplementary Figure 10 compares frequency histograms of the number of domains in 15 runs at various t_{MC}, confirming the ability of the tiles to slow down domain coarsening, in line with experimental findings outlined in Figure 3.

Despite its coarse-grained nature, simulations offer insights on the different mechanisms leading to domain coarsening and on how these are influenced by the presence of DOLAs. Generally, we observed coarsening followed two distinct pathways: domain coalescence and Ostwald ripening.[70] Simulations suggest that the presence of tiles slows down the former mechanism, by offering a steric barrier that prevents the interfaces of two distinct domains from coming in sufficient proximity and undergo coalescence. Instead, Ostwald ripening, supported by the exchange of particles (spins) between domains via diffusion through the background phase, occurs regardless of the presence of tiles. This second coarsening process is solely responsible for the decrease in total line length observed in the presence of tiles at very long simulation times (Figure 4d, inset), when no further domain coalescence is observed. In experiments, tile-decorated GUVs display stable

https://doi.org/10.1021/jacs.3c01493
J. Am. Chem. Soc. 2023, 145, 11265−11275

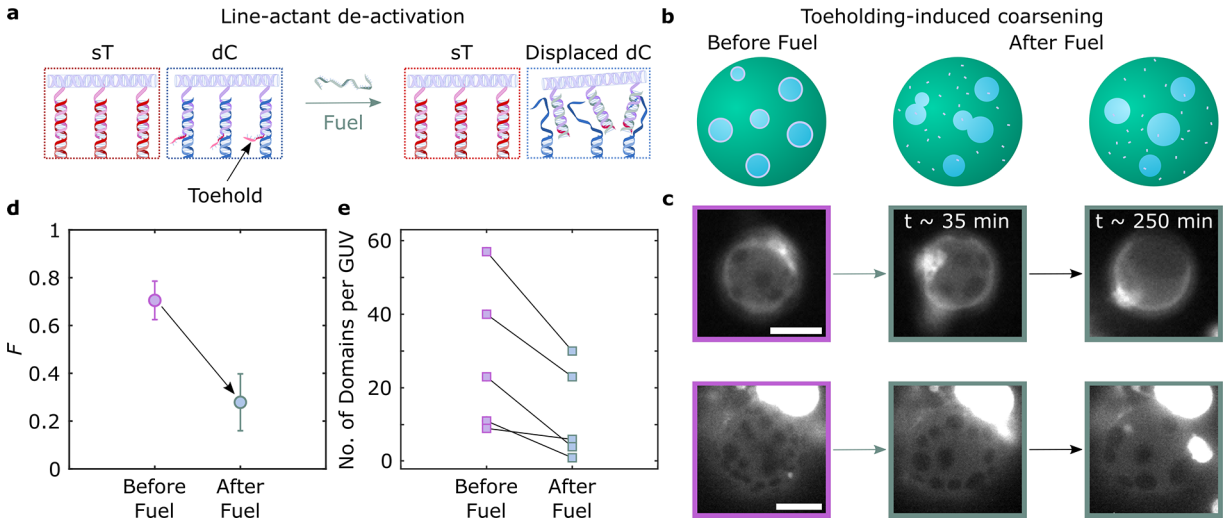

Figure 5. Toehold-mediated strand displacement enables dynamic control over membrane lateral organization via DOLA reconfiguration. (a) Schematic depiction of anchor-points in DOLAs, highlighting the toehold domain linked to the dC-targeting overhangs. The addition of a fuel strand catalyzes a strand displacement reaction, detaching the DNA tile from the anchor-points and leading to DOLA deactivation. (b) DOLA reconfiguration and their subsequent desorption from line-interfaces lead to domain coarsening. (c) Representative epi-fluorescence micrographs acquired before and after (~35 and ~250 min) the addition of fuel, demonstrating domain coarsening triggered by DOLA deactivation. Fluorescent marker is Texas Red-DHPE, which partitions to the L_d phase. Scale bars = 10 μm. (d) Influence of DOLA reconfiguration on the fraction, F, of GUVs exhibiting more than two domains with respect to that of Janus-like vesicles before (n = 60 vesicles) and after (~250 min, n = 74 vesicles) the addition of fuel. (e) Number of domains per GUV in 6 representative vesicles, showing the effect of toeholding before and after (~250 min) the addition of fuel. Points connected by lines are relative to the same GUV.

2D Pickering emulsions ~3 h after quenching, when most nonfunctinonalized vesicles have fully equilibrated (Figure 3b), hinting that domain coalescence may be the primary mechanism leading to coarsening, with Ostwald ripening playing a comparatively minor role.

Figure 4d compares the simulated time-evolution of the overall line-interface length (L) for systems featuring each DOLA design with those lacking tiles. At late simulation times, the interface length is higher for 24×, followed by 12× and 6×, with the latter design showing values identical to the tileless control, confirming the expected link between the number of anchors and line-stabilizing ability. See also Supplementary Figure 11 and the associated Supplementary Movies 4 and 5 for representative simulation runs with 24× and 6× DOLAs.

Consistently, as shown in Figure 4e, the simulated tile-occupied fraction of the line (ϕ) converges to values that monotonically increase with the number of anchors, in agreement with the experimental/theoretical findings outlined in Figure 2d. Analogous trends are noted when monitoring the time-dependent fraction of tiles at the line-interface, found to increase with anchor-point number (Supplementary Figure 13). Further insights can be gathered from Figure 4f, where we plot the fraction of tiles at the line as a function of interface length. We note that, as L decreases due to domain coarsening, strongly binding 24× tiles remain more persistently pinned at the interface, while 6× tiles are readily expelled. Finally, in Figure 4g, we explicitly explore the correlation between ϕ and line length. As L shrinks, a plateau in ϕ is approached for 6× tiles able to readily desorb from the line, while a correlation is retained for strongly pinned 24× DOLAs.

Fueling Lipid Domain Reorganization with Dynamic DNA Line-Actants. The ability of DOLAs to regulate domain coarsening can be readily coupled to nanostructure reconfigurability afforded by toeholding reactions,[71−73] thus enabling dynamic control over membrane lateral organization. To demonstrate this functionality, 12× line-actants were modified with a 6-nt toehold domain of sequence α on the 3′-end of cholesterol-targeting overhangs (see Supplementary Table 9). As depicted schematically in Figure 5a, a chemical fuel, in the form of an oligonucleotide with sequence $\alpha^*\delta 2$, can selectively displace the dC-anchoring modules from the tile through a toeholding reaction (see Supplementary Figure 14 for an agarose gel confirming the sought molecular response). When removing the dC anchors, DOLAs are expected to lose their line-interface affinity and instead partition to L_d driven by the remaining sT moieties, negating the ability of the tiles to stabilize lipid domains.

As sketched in Figure 5b (left) and shown in Figure 5c (left) with fluorescence micrographs, GUVs decorated with the responsive 12× tiles form stable 2D emulsions when subjected to the heating−cooling cycle outlined above. Figure 5b,c (center and right) show domain coarsening triggered by exposure to the fuel strand, which translates into a clear decrease in the fraction F of non-Janus GUVs, shown in Figure 5d. The series of snapshots in Figure 5c show that, while some GUVs acquire a Janus morphology after fuel exposure (top), others retain a larger number of domains. Nonetheless, all observed GUVs experience a substantial degree of domain coarsening, as outlined in Figure 5e, where we track changes in the number of domains following fuel addition in individual GUVs. As exemplified in Supplementary Figure 15, domains often bulge after fuel addition, possibly due to a slight osmolarity mismatch coupled with differences in spontaneous curvature between the phases. Bulging may in turn be responsible for enhancing stability against coalescence of the domains after line-actant deactivation, preventing some GUVs from relaxing into the Janus configuration.[74]

Responsive DOLAs for Domain Fission in Synthetic Membranes. Reversible domain stabilization with DOLAs can be exploited to synthetically replicate the action of

https://doi.org/10.1021/jacs.3c01493
J. Am. Chem. Soc. 2023, 145, 11265−11275

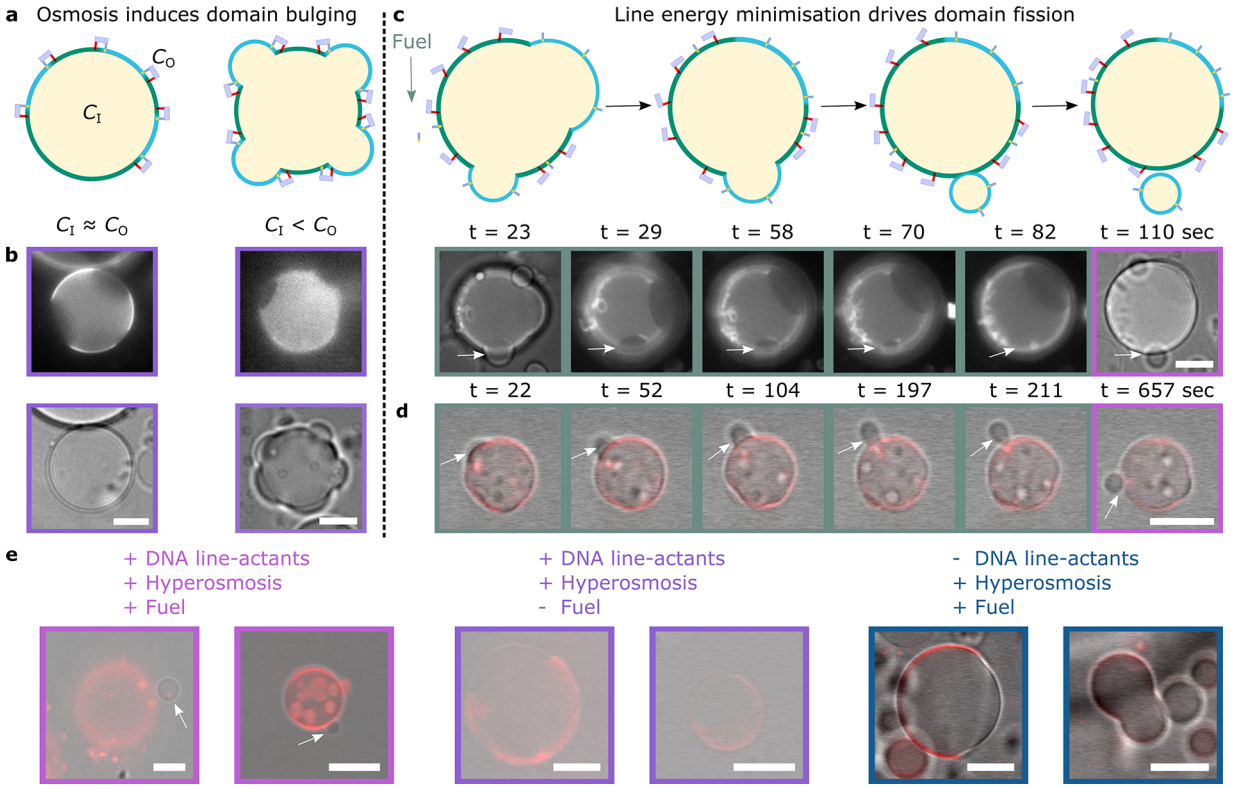

Figure 6. Biomimetic fission pathway mediated by DOLAs. The fission mechanism requires two sequential processes: domain budding and domain fission. (a) Schematic representation of the initial step, where bulging-out of DOLA-stabilized domains is caused by hyperosmotic shock, i.e., by increasing the outer concentration of solutes (C_O) relative to the concentration inside the GUVs (C_I). (b) Epifluorescence (top) and bright-field (bottom) micrographs of representative GUVs exposed to iso-osmolar ($C_I \approx C_O$) or hyper-osmolar ($C_I < C_O$) environments, showing respectively spherical or bulging-out morphologies. (c) (Top) Schematic depiction of the second step, where fuel addition and tile desorption from the interfaces induce budding off or fission of the protruding domains. (Bottom) Evolution of L_o-domain fission in a representative liposome observed with bright-field and epifluorescence microscopy (see Supplementary Movie 6). Time-stamps refer to the time elapsed after initial acquisition. Fuel was added ~2 min before acquisition began. (d) Evolution of L_o-domain fission in a representative GUV shown with overlaid confocal and bright-field images (see Supplementary Movie 7). Time-stamps refer to the time elapsed after initial acquisition. Fuel was added ~90 min before acquisition began. (e) Overlaid confocal and bright-field micrographs of representative liposomes when exposed to hyper-osmotic environments containing fuel (left) or lacking fuel (middle) or in the presence of fuel but lacking DNA line-actants (right). Fluorescent marker is Texas Red-DHPE, which partitions to the L_d phase. All scale bars = 10 μm.

biological membrane-remodeling machinery, tackling a critical bottleneck in synthetic-cell engineering.[75] For instance, phospholipase A_2 has been postulated to exhibit enhanced catalytic activity at line-interfaces between coexisting L_d–L_o phases, driving domain budding and fission.[76] We propose our line-actants could form the basis of an analogous pathway coordinating fission and, therefore, three-dimensional membrane transformation.

We prepared GUVs in an initial configuration featuring DOLA-stabilized microdomains, as outlined above. We then applied a hyper-osmotic shock by increasing the osmolarity of the outside solution (C_O) to ~1.28 × C_I, where C_I is the internal vesicle osmolarity, thus leading to an increase in GUV excess area.[77] While in some cases hyperosmosis led to membrane internalization (Supplementary Figure 16), some domains responded by bulging-out, as depicted in Figure 6a and experimentally observed in Figure 6b. At this stage, some bulged-out domains could be "primed" for complete budding-off or fission, driven by minimization of line-interface energy and opposed by membrane fluctuation entropy[78] and, possibly, steric repulsion between DOLAs preventing line shrinkage. Deactivation of the line-actants through fuel strand addition is expected to increase line tension and negate any steric hindrance to interface shrinkage, tipping the marginally stable domains into full budding-off and fission (Figure 6c, top). Fission events can be promptly recorded experimentally upon fuel-strand addition, as shown in Supplementary Movie 6 and Figure 6c (bottom). The sequence of epifluorescence images in the latter clearly shows the dark region corresponding to a budding L_o-domain shrinking progressively and ultimately disappearing. Vesicle fission is confirmed with bright-field micrographs, where arrows highlight both the "parent" and "offspring" vesicles regaining spherical morphologies. An analogous example is provided in Figure 6d and the associated Supplementary Movie 7, with overlaid confocal and bright-field micrographs.

In further support of our proposed synthetic fission pathway, DOLA-functionalized liposomes with stabilized microdomains were gently added to imaging wells containing hyper-osmotic buffer baths with and without fuel. In the former scenario, confocal microscopy revealed further examples of phase-separated GUVs found in proximity of a smaller single-phase vesicle (Figure 6e, left, and Supplementary Figure 17), similar to the confirmed fission occurrences shown in Figure 6c and d. In turn, we did not observe such presumed fission events in vesicles immersed in baths lacking fuel (Figure 6e, middle),

https://doi.org/10.1021/jacs.3c01493
J. Am. Chem. Soc. 2023, 145, 11265−11275

where GUVs appeared more Janus-like, also in line with our findings on sample heterogeneity summarized in Supplementary Figure 16. Finally, DOLA-lacking GUVs, immersed in fuel-supplemented hyper-osmotic buffer, simply adopted dumbbell shapes thanks to their Janus morphology (Figure 6e, right), consistent with the expectation that the used C_O/C_I is insufficient to drive fission of quasi-hemispherical domains.[79]

CONCLUSIONS AND OUTLOOK

In summary, we presented DNA origami nanostructures—dubbed DOLAs—designed rationally to accumulate at the one-dimensional line-interface between lipid domains, imitating biological line-active membrane inclusions. The synthetic line-actants exploit the programmability and modularity of DNA origami, combined with the natural tendency of cholesterol and tocopherol "anchors" to enrich distinct lipid phases. Through experiments and numerical modeling, we demonstrated that the affinity for line-interfaces can be programmed by tuning the number of hydrophobic anchors, thus outlining a general design principle readily applicable to different origami designs, hydrophobic groups, or membrane compositions. We further demonstrated that our line-actants are able to stabilize small lipid domains against coarsening, giving rise to two-dimensional analogues of Pickering emulsions on the surface of giant liposomes and achieving a previously unattainable degree of control over the lateral organization of synthetic bilayers.

The nanodevices can be externally deactivated through a toehold-mediated strand displacement operation, triggering domain coalescence. Coarse-grained Monte Carlo simulations replicate the experimental phenomenology, identifying origami−origami steric repulsion as the primary mechanism leading to domain stabilization and ultimately validating our line-actant engineering strategy. Finally, we combined externally triggered line-actant deactivation with osmotic unbalance to implement a proof-of-concept synthetic fission pathway, whereby offspring liposomes programmably bud-off from parent vesicles, demonstrating the ability of the nanodevices to promote large-scale membrane restructuring similar to biological nanomachines.[23,80,81]

The simplicity and modularity of the mechanism underpinning line-action in our devices point at possible design variations that exploit different origami geometries, anchor chemistry, and polymerization approaches to further program the number, size, and morphology of lipid domains, marking a conceptual shift in synthetic-membrane engineering. Responsiveness to a wider range of physical and chemical stimuli can also be achieved by incorporating active elements such as DNAzymes,[82] G-quadruplexes,[83] aptamers,[84] and/or photoactuable moieties (e.g., azobenzene),[85] thus broadening the design space and applicability of synthetic membrane-restructuring pathways.

Thanks to their ability to program membrane restructuring and the lateral distribution of membrane inclusions, the DOLAs constitute a valuable toolkit in synthetic-cell science that could underpin elusive and highly sought-after behaviors such as synthetic-cell division, vesicle-based trafficking, and signal transduction pathways, ultimately unlocking disruptive applications to advance therapeutics and diagnostics.

Finally, DOLAs could be used to exert control over the local domain structure of living-cell membranes. One could thus envisage applying the origami line-actant toolkit as the basis of biophysical studies aimed at clarifying the role of microphase separation in cell signaling, by triggering the formation and disruption of "lipid rafts" at will.[20] If strong correlations between disease-related pathways and membrane-domain structure are established, the origami line-actants could carry potential therapeutic value by unlocking a previously unattainable strategy for conditioning cell behavior.

ASSOCIATED CONTENT

Supporting Information

The Supporting Information is available free of charge at https://pubs.acs.org/doi/10.1021/jacs.3c01493.

Experimental methods, supplementary notes, supplementary figures, supplementary table with parameters for model and simulations, DNA sequences of the nanostructures used throughout this work (PDF)

Movie S1: Representative simulation trajectory with 12× DNA-origami line-actants following the system after quenching for 2×10^7 MC cycles. Box size: 320 × 372 lattice points (AVI)

Movie S2: Representative simulation trajectory with 12× DNA-origami line-actants following the system after quenching for 3×10^7 MC cycles. Box size: 160 × 172 lattice points (AVI)

Movie S3: Representative simulation trajectory lacking DNA-origami line-actants following the system after quenching for 3×10^7 MC cycles. Box size: 160 × 172 lattice points (AVI)

Movie S4: Representative simulation trajectory with 24× DNA-origami line-actants following the system after quenching for 3×10^7 MC cycles. Box size: 160 × 172 lattice points (AVI)

Movie S5: Representative simulation trajectory with 6× DNA-origami line-actants following the system after quenching for 3×10^7 MC cycles. Box size: 160 × 172 lattice points.(AVI)

Movie S6: Evolution of L_o-domain fission event in a representative vesicle observed with bright-field and *epi*-fluorescence microscopy. Time-stamps refer to the time elapsed after initial acquisition. Fuel was added 2 min before acquisition began. The fluorescent marker is TexasRed-DHPE, which labels the L_d phase. Scale bar: 10 μm (AVI)

Movie S7: Evolution of L_o-domain fission event in a representative vesicle observed with overlaid confocal and bright-field microscopy. Time-stamps refer to the time elapsed after initial acquisition. Fuel was added 90 min before acquisition began. The fluorescent marker is TexasRed-DHPE, which labels the L_d phase. Scale bar: 10 μm (AVI)

AUTHOR INFORMATION

Corresponding Authors

Roger Rubio-Sánchez − *Department of Chemical Engineering and Biotechnology, University of Cambridge, Cambridge CB3 0AS, United Kingdom; Department of Chemistry, Molecular Sciences Research Hub, Imperial College London, London W12 0BZ, United Kingdom; fabriCELL, Molecular Sciences Research Hub, Imperial College London, London W12 0BZ, United Kingdom; Biological and Soft Systems, Cavendish Laboratory, University of Cambridge, Cambridge CB3 0HE, United Kingdom;* orcid.org/0000-0001-5574-5809; Email: rmr44@cam.ac.uk

https://doi.org/10.1021/jacs.3c01493
J. Am. Chem. Soc. 2023, 145, 11265−11275

Lorenzo Di Michele − *Department of Chemical Engineering and Biotechnology, University of Cambridge, Cambridge CB3 0AS, United Kingdom; Department of Chemistry, Molecular Sciences Research Hub, Imperial College London, London W12 0BZ, United Kingdom; fabriCELL, Molecular Sciences Research Hub, Imperial College London, London W12 0BZ, United Kingdom; Biological and Soft Systems, Cavendish Laboratory, University of Cambridge, Cambridge CB3 0HE, United Kingdom;* orcid.org/0000-0002-1458-9747; Email: ld389@cam.ac.uk

Authors

Bortolo Matteo Mognetti − *Interdisciplinary Center for Nonlinear Phenomena and Complex Systems, Université Libre de Bruxelles (ULB), B-1050 Brussels, Belgium;* orcid.org/0000-0002-7960-8224

Pietro Cicuta − *Biological and Soft Systems, Cavendish Laboratory, University of Cambridge, Cambridge CB3 0HE, United Kingdom;* orcid.org/0000-0002-9193-8496

Complete contact information is available at: https://pubs.acs.org/10.1021/jacs.3c01493

Notes

The authors declare no competing financial interest.

■ ACKNOWLEDGMENTS

R.R.S. acknowledges support from the EPSRC CDT in Nanoscience and Nanotechnology (NanoDTC, Grant No. EP/L015978/1), the Mexican National Council for Science and Technology, and the Cambridge Trust. L.D.M. acknowledges support from a Royal Society University Research Fellowship (UF160152, URF\R\221009). R.R.S. and L.D.M. also acknowledge funding from the Royal Society Research Fellows Enhanced Research Expenses (RF/ERE/210029) and from the European Research Council (ERC) under the Horizon 2020 Research and Innovation Programme (ERC-STG No 851667 NANOCELL). The authors acknowledge computational resources provided by the Consortium des Équipements de Calcul Intensif (CÉCI), funded by the Fonds de la Recherche Scientifique de Belgique (F.R.S.-FNRS) under Grant No. 2.5020.11 and by the Walloon Region. A dataset in support of this work can be accessed free of charge at 10.17863/CAM.94868

■ REFERENCES

(1) Alberts, B. *Molecular Biology of the Cell*, sixth ed.; Garland Science: New York, 2017.
(2) Veatch, S. L.; Cicuta, P.; Sengupta, P.; Honerkamp-Smith, A.; Holowka, D.; Baird, B. Critical Fluctuations in Plasma Membrane Vesicles. *ACS Chem. Biol.* **2008**, *3*, 287−293.
(3) Baumgart, T.; Hammond, A. T.; Sengupta, P.; Hess, S. T.; Holowka, D. A.; Baird, B. A.; Webb, W. W. Large-scale fluid/fluid phase separation of proteins and lipids in giant plasma membrane vesicles. *Proc. Natl. Acad. Sci. U. S. A.* **2007**, *104*, 3165−3170.
(4) Honerkamp-Smith, A. R.; Veatch, S. L.; Keller, S. L. An introduction to critical points for biophysicists; observations of compositional heterogeneity in lipid membranes. *Biochim. Biophys. Acta Biomembr.* **2009**, *1788*, 53−63.
(5) Veatch, S. L.; Cicuta, P. In *Physics of Biological Membranes*; Bassereau, P., Sens, P., Eds.; Springer International Publishing: Cham, 2018; pp 141−168.
(6) Shaw, T. R.; Ghosh, S.; Veatch, S. L. Critical Phenomena in Plasma Membrane Organization and Function. *Annu. Rev. Phys. Chem.* **2021**, *72*, 51−72.
(7) Cammarota, E.; Soriani, C.; Taub, R.; Morgan, F.; Sakai, J.; Veatch, S. L.; Bryant, C. E.; Cicuta, P. Criticality of plasma membrane lipids reflects activation state of macrophage cells. *J. R. Soc. Interface* **2020**, *17*, 20190803.
(8) Gray, E. M.; Díaz-Vázquez, G.; Veatch, S. L. Growth Conditions and Cell Cycle Phase Modulate Phase Transition Temperatures in RBL-2H3 Derived Plasma Membrane Vesicles. *PLoS One* **2015**, *10*, e0137741.
(9) Frechin, M.; Stoeger, T.; Daetwyler, S.; Gehin, C.; Battich, N.; Damm, E.-M.; Stergiou, L.; Riezman, H.; Pelkmans, L. Cell-intrinsic adaptation of lipid composition to local crowding drives social behaviour. *Nature* **2015**, *523*, 88−91.
(10) Ernst, R.; Ballweg, S.; Levental, I. Cellular mechanisms of physicochemical membrane homeostasis. *Curr. Opin. Cell Biol.* **2018**, *53*, 44−51.
(11) Weise, K.; Triola, G.; Brunsveld, L.; Waldmann, H.; Winter, R. Influence of the Lipidation Motif on the Partitioning and Association of N-Ras in Model Membrane Subdomains. *J. Am. Chem. Soc.* **2009**, *131*, 1557−1564.
(12) Weise, K.; Triola, G.; Janosch, S.; Waldmann, H.; Winter, R. Visualizing association of lipidated signaling proteins in heterogeneous membranes Partitioning into subdomains, lipid sorting, interfacial adsorption, and protein association. *Biochim. Biophys. Acta Biomembr.* **2010**, *1798*, 1409−1417.
(13) Weise, K.; Kapoor, S.; Denter, C.; Nikolaus, J.; Opitz, N.; Koch, S.; Triola, G.; Herrmann, A.; Waldmann, H.; Winter, R. Membrane-Mediated Induction and Sorting of K-Ras Microdomain Signaling Platforms. *J. Am. Chem. Soc.* **2011**, *133*, 880−887.
(14) Lin, X.; Gorfe, A. A.; Levental, I. Protein Partitioning into Ordered Membrane Domains: Insights from Simulations. *Biophys. J.* **2018**, *114*, 1936−1944.
(15) Nicolini, C.; Baranski, J.; Schlummer, S.; Palomo, J.; Lumbierres-Burgues, M.; Kahms, M.; Kuhlmann, J.; Sanchez, S.; Gratton, E.; Waldmann, H.; Winter, R. Visualizing Association of N-Ras in Lipid Microdomains: Influence of Domain Structure and Interfacial Adsorption. *J. Am. Chem. Soc.* **2006**, *128*, 192−201.
(16) García-Sáez, A. J.; Chiantia, S.; Schwille, P. Effect of Line Tension on the Lateral Organization of Lipid Membranes. *J. Biol. Chem.* **2007**, *282*, 33537−33544.
(17) García-Sáez, A. J.; Chiantia, S.; Salgado, J.; Schwille, P. Pore Formation by a Bax-Derived Peptide: Effect on the Line Tension of the Membrane Probed by AFM. *Biophys. J.* **2007**, *93*, 103−112.
(18) Schmid, F. Physical mechanisms of micro- and nanodomain formation in multicomponent lipid membranes. *Biochim. Biophys. Acta Biomembr.* **2017**, *1859*, 509−528.
(19) Lingwood, D.; Simons, K. Lipid Rafts As a Membrane-Organizing Principle. *Science* **2010**, *327*, 46−50.
(20) Simons, K.; Toomre, D. Lipid rafts and signal transduction. *Nat. Rev. Mol. Cell Biol.* **2000**, *1*, 31.
(21) Shelby, S. A.; Castello-Serrano, I.; Wisser, K. C.; Levental, I.; Veatch, S. L. Membrane phase separation drives organization at B cell receptor clusters. *bioRxiv* 2021, DOI: 10.1101/2021.05.12.443834, accessed on 2022−08−08.
(22) Booth, A.; Marklew, C. J.; Ciani, B.; Beales, P. A. The influence of phosphatidylserine localisation and lipid phase on membrane remodelling by the ESCRT-II/ESCRT-III complex. *Faraday Discuss.* **2021**, *232*, 188−202.
(23) Kim, J. H.; Singh, A.; Del Poeta, M.; Brown, D. A.; London, E. The effect of sterol structure upon clathrin-mediated and clathrin-independent endocytosis. *J. Cell Sci.* **2017**, *130*, 2682−2695.
(24) Buddingh', B. C.; van Hest, J. C. M. Artificial Cells: Synthetic Compartments with Life-like Functionality and Adaptivity. *Acc. Chem. Res.* **2017**, *50*, 769−777.
(25) Noireaux, V.; Maeda, Y. T.; Libchaber, A. Development of an artificial cell, from self-organization to computation and self-reproduction. *Proc. Natl. Acad. Sci. U.S.A.* **2011**, *108*, 3473−3480.
(26) Emir Diltemiz, S.; Tavafoghi, M.; de Barros, N. R.; Kanada, M.; Heinämäki, J.; Contag, C.; Seidlits, S. K.; Ashammakhi, N. Use of

artificial cells as drug carriers. *Mater. Chem. Front.* **2021**, *5*, 6672−6692.
(27) Zhang, Y.; Ruder, W. C.; LeDuc, P. R. Artificial cells: building bioinspired systems using small-scale biology. *Trends Biotechnol.* **2008**, *26*, 14−20.
(28) Xu, C.; Hu, S.; Chen, X. Artificial cells: from basic science to applications. *Mater. Today* **2016**, *19*, 516−532.
(29) Trantidou, T.; Friddin, M.; Elani, Y.; Brooks, N. J.; Law, R. V.; Seddon, J. M.; Ces, O. Engineering Compartmentalized Biomimetic Micro- and Nanocontainers. *ACS Nano* **2017**, *11*, 6549−6565.
(30) Hindley, J. W.; Law, R. V.; Ces, O. Membrane functionalization in artificial cell engineering. *SN Appl. Sci.* **2020**, *2*, 593.
(31) Hindley, J. W.; Zheleva, D. G.; Elani, Y.; Charalambous, K.; Barter, L. M. C.; Booth, P. J.; Bevan, C. L.; Law, R. V.; Ces, O. Building a synthetic mechanosensitive signaling pathway in compartmentalized artificial cells. *Proc. Natl. Acad. Sci. U. S. A.* **2019**, *116*, 16711−16716.
(32) Hindley, J. W.; Elani, Y.; McGilvery, C. M.; Ali, S.; Bevan, C. L.; Law, R. V.; Ces, O. Light-triggered enzymatic reactions in nested vesicle reactors. *Nat. Commun.* **2018**, *9*, 1093.
(33) Lee, K. Y.; Park, S.-J.; Lee, K. A.; Kim, S.-H.; Kim, H.; Meroz, Y.; Mahadevan, L.; Jung, K.-H.; Ahn, T. K.; Parker, K. K.; Shin, K. Photosynthetic artificial organelles sustain and control ATP-dependent reactions in a protocellular system. *Nat. Biotechnol.* **2018**, *36*, 530−535.
(34) Altamura, E.; Milano, F.; Tangorra, R. R.; Trotta, M.; Omar, O. H.; Stano, P.; Mavelli, F. Highly oriented photosynthetic reaction centers generate a proton gradient in synthetic protocells. *Proc. Natl. Acad. Sci. U. S. A.* **2017**, *114*, 3837−3842.
(35) Litschel, T.; Ramm, B.; Maas, R.; Heymann, M.; Schwille, P. Beating Vesicles: Encapsulated Protein Oscillations Cause Dynamic Membrane Deformations. *Angew. Chem., Int. Ed.* **2018**, *57*, 16286−16290.
(36) Seeman, N. C.; Sleiman, H. F. DNA nanotechnology. *Nature Reviews Materials* **2018**, *3*, 17068.
(37) Beales, P. A.; Vanderlick, T. K. Application of nucleic acid−lipid conjugates for the programmable organisation of liposomal modules. *Adv. Colloid Interface Sci.* **2014**, *207*, 290−305.
(38) Langecker, M.; Arnaut, V.; List, J.; Simmel, F. C. DNA Nanostructures Interacting with Lipid Bilayer Membranes. *Acc. Chem. Res.* **2014**, *47*, 1807−1815.
(39) Rubio-Sánchez, R.; Fabrini, G.; Cicuta, P.; Di Michele, L. Amphiphilic DNA nanostructures for bottom-up synthetic biology. *Chem. Commun.* **2021**, *57*, 12725−127405.
(40) Sobota, D.; Joshi, H.; Ohmann, A.; Aksimentiev, A.; Keyser, U. F. Tailoring Interleaflet Lipid Transfer with a DNA-based Synthetic Enzyme. *Nano Lett.* **2020**, *20*, 4306−4311.
(41) Ohmann, A.; Li, C.-Y.; Maffeo, C.; Al Nahas, K.; Baumann, K. N.; Göpfrich, K.; Yoo, J.; Keyser, U. F.; Aksimentiev, A. A synthetic enzyme built from DNA flips 107 lipids per second in biological membranes. *Nat. Commun.* **2018**, *9*, 2426.
(42) Morzy, D.; Rubio-Sánchez, R.; Joshi, H.; Aksimentiev, A.; Di Michele, L.; Keyser, U. F. Cations regulate membrane-attachment and functionality of DNA nanostructures. *J. Am. Chem. Soc.* **2021**, *143*, 7358−7367.
(43) Chidchob, P.; Offenbartl-Stiegert, D.; McCarthy, D.; Luo, X.; Li, J.; Howorka, S.; Sleiman, H. F. Spatial Presentation of Cholesterol Units on a DNA Cube as a Determinant of Membrane Protein-Mimicking Functions. *J. Am. Chem. Soc.* **2019**, *141*, 1100−1108.
(44) Fragasso, A.; De Franceschi, N.; Stömmer, P.; van der Sluis, E. O.; Dietz, H.; Dekker, C. Reconstitution of Ultrawide DNA Origami Pores in Liposomes for Transmembrane Transport of Macromolecules. *ACS Nano* **2021**, *15*, 12768−12779.
(45) Diederichs, T.; Pugh, G.; Dorey, A.; Xing, Y.; Burns, J. R.; Hung Nguyen, Q.; Tornow, M.; Tampé, R.; Howorka, S. Synthetic protein-conductive membrane nanopores built with DNA. *Nat. Commun.* **2019**, *10*, 5018.
(46) Amjad, O. A.; Mognetti, B. M.; Cicuta, P.; Di Michele, L. Membrane Adhesion through Bridging by Multimeric Ligands. *Langmuir* **2017**, *33*, 1139−1146.
(47) Mognetti, B. M.; Cicuta, P.; Di Michele, L. Programmable interactions with biomimetic DNA linkers at fluid membranes and interfaces. *Rep. Prog. Phys.* **2019**, *82*, 116601.
(48) Parolini, L.; Kotar, J.; Di Michele, L.; Mognetti, B. M. Controlling Self-Assembly Kinetics of DNA-Functionalized Liposomes Using Toehold Exchange Mechanism. *ACS Nano* **2016**, *10*, 2392−2398.
(49) Parolini, L.; Mognetti, B. M.; Kotar, J.; Eiser, E.; Cicuta, P.; Di Michele, L. Volume and porosity thermal regulation in lipid mesophases by coupling mobile ligands to soft membranes. *Nat. Commun.* **2015**, *6*, 5948.
(50) Beales, P. A.; Nam, J.; Vanderlick, T. K. Specific adhesion between DNA-functionalized "Janus" vesicles: size-limited clusters. *Soft Matter* **2011**, *7*, 1747−1755.
(51) Kaufhold, W. T.; Brady, R. A.; Tuffnell, J. M.; Cicuta, P.; Di Michele, L. Membrane Scaffolds Enhance the Responsiveness and Stability of DNA-Based Sensing Circuits. *Bioconjugate Chem.* **2019**, *30*, 1850−1859.
(52) Walczak, M.; Brady, R. A.; Mancini, L.; Contini, C.; Rubio-Sánchez, R.; Kaufhold, W. T.; Cicuta, P.; Di Michele, L. Responsive core-shell DNA particles trigger lipid-membrane disruption and bacteria entrapment. *Nat. Commun.* **2021**, *12*, 4743.
(53) Journot, C. M. A.; Ramakrishna, V.; Wallace, M. I.; Turberfield, A. J. Modifying Membrane Morphology and Interactions with DNA Origami Clathrin-Mimic Networks. *ACS Nano* **2019**, *13*, 9973−9979.
(54) Franquelim, H. G.; Khmelinskaia, A.; Sobczak, J.-P.; Dietz, H.; Schwille, P. Membrane sculpting by curved DNA origami scaffolds. *Nat. Commun.* **2018**, *9*, 811.
(55) Franquelim, H. G.; Dietz, H.; Schwille, P. Reversible membrane deformations by straight DNA origami filaments. *Soft Matter* **2021**, *17*, 276−287.
(56) Rubio-Sánchez, R.; Barker, S. E.; Walczak, M.; Cicuta, P.; Di Michele, L. A Modular, Dynamic, DNA-Based Platform for Regulating Cargo Distribution and Transport between Lipid Domains. *Nano Lett.* **2021**, *21*, 2800−2808.
(57) Schade, M.; Knoll, A.; Vogel, A.; Seitz, O.; Liebscher, J.; Huster, D.; Herrmann, A.; Arbuzova, A. Remote Control of Lipophilic Nucleic Acids Domain Partitioning by DNA Hybridization and Enzymatic Cleavage. *J. Am. Chem. Soc.* **2012**, *134*, 20490−20497.
(58) Czogalla, A.; Petrov, E. P.; Kauert, D. J.; Uzunova, V.; Zhang, Y.; Seidel, R.; Schwille, P. Switchable domain partitioning and diffusion of DNA origami rods on membranes. *Faraday Discuss.* **2013**, *161*, 31−43.
(59) Avakyan, N.; Conway, J. W.; Sleiman, H. F. Long-Range Ordering of Blunt-Ended DNA Tiles on Supported Lipid Bilayers. *J. Am. Chem. Soc.* **2017**, *139*, 12027−12034.
(60) Schindelin, J.; et al. Fiji: an open-source platform for biological-image analysis. *Nat. Methods* **2012**, *9*, 676−682.
(61) Schnitzbauer, J.; Strauss, M. T.; Schlichthaerle, T.; Schueder, F.; Jungmann, R. Super-resolution microscopy with DNA-PAINT. *Nat. Protoc.* **2017**, *12*, 1198−1228.
(62) Strauss, M. T.; Schueder, F.; Haas, D.; Nickels, P. C.; Jungmann, R. Quantifying absolute addressability in DNA origami with molecular resolution. *Nat. Commun.* **2018**, *9*, 1600.
(63) Clowsley, A. H.; Kaufhold, W. T.; Lutz, T.; Meletiou, A.; Di Michele, L.; Soeller, C. Detecting Nanoscale Distribution of Protein Pairs by Proximity-Dependent Super-resolution Microscopy. *J. Am. Chem. Soc.* **2020**, *142*, 12069−12078.
(64) Clowsley, A. H.; Kaufhold, W. T.; Lutz, T.; Meletiou, A.; Di Michele, L.; Soeller, C. Repeat DNA-PAINT suppresses background and non-specific signals in optical nanoscopy. *Nat. Commun.* **2021**, *12*, 501.
(65) Snodin, B. E. K.; Schreck, J. S.; Romano, F.; Louis, A. A.; Doye, J. P. K. Coarse-grained modelling of the structural properties of DNA origami. *Nucleic Acids Res.* **2019**, *47*, 1585−1597.

(66) Sample, M.; Matthies, M.; Šulc, P. Hairygami: Analysis of DNA Nanostructure's Conformational Change Driven by Functionalizable Overhangs. *arXiv* 2023, DOI: 10.48550/arXiv.2302.09109, accessed on 2023−03−24.
(67) Honerkamp-Smith, A. R.; Cicuta, P.; Collins, M. D.; Veatch, S. L.; den Nijs, M.; Schick, M.; Keller, S. L. Line Tensions, Correlation Lengths, and Critical Exponents in Lipid Membranes Near Critical Points. *Biophys. J.* **2008**, *95*, 236−246.
(68) Veatch, S. L.; Keller, S. L. Separation of Liquid Phases in Giant Vesicles of Ternary Mixtures of Phospholipids and Cholesterol. *Biophys. J.* **2003**, *85*, 3074−3083.
(69) Landau, D.; Binder, K. *A Guide to Monte Carlo Simulations in Statistical Physics*; Cambridge University Press, 2021; pp 51−70.
(70) Stanich, C.; Honerkamp-Smith, A.; Putzel, G.; Warth, C.; Lamprecht, A.; Mandal, P.; Mann, E.; Hua, T.-A.; Keller, S. Coarsening Dynamics of Domains in Lipid Membranes. *Biophys. J.* **2013**, *105*, 444−454.
(71) Zhang, D. Y.; Winfree, E. Control of DNA Strand Displacement Kinetics Using Toehold Exchange. *J. Am. Chem. Soc.* **2009**, *131*, 17303−17314.
(72) Zhang, D. Y.; Seelig, G. Dynamic DNA nanotechnology using strand-displacement reactions. *Nat. Chem.* **2011**, *3*, 103.
(73) Simmel, F. C.; Yurke, B.; Singh, H. R. Principles and Applications of Nucleic Acid Strand Displacement Reactions. *Chem. Rev.* **2019**, *119*, 6326−6369.
(74) Ursell, T. S.; Klug, W. S.; Phillips, R. Morphology and interaction between lipid domains. *Proc. Natl. Acad. Sci. U. S. A.* **2009**, *106*, 13301−13306.
(75) Kretschmer, S.; Ganzinger, K. A.; Franquelim, H. G.; Schwille, P. Synthetic cell division via membrane-transforming molecular assemblies. *BMC Biology* **2019**, *17*, 43.
(76) Staneva, G.; Angelova, M. I.; Koumanov, K. Phospholipase A2 promotes raft budding and fission from giant liposomes. *Chem. Phys. Lipids* **2004**, *129*, 53−62.
(77) Steinkühler, J.; Knorr, R. L.; Zhao, Z.; Bhatia, T.; Bartelt, S. M.; Wegner, S.; Dimova, R.; Lipowsky, R. Controlled division of cell-sized vesicles by low densities of membrane-bound proteins. *Nat. Commun.* **2020**, *11*, 905.
(78) Lipowsky, R. Budding of membranes induced by intramembrane domains. *J. Phys. II France* **1992**, *2*, 1825−1840.
(79) Dreher, Y.; Jahnke, K.; Bobkova, E.; Spatz, J. P.; Göpfrich, K. Division and Regrowth of Phase-Separated Giant Unilamellar Vesicles. *Angew. Chem., Int. Ed.* **2021**, *60*, 10661−10669.
(80) Carman, P. J.; Dominguez, R. BAR domain proteins-a linkage between cellular membranes, signaling pathways, and the actin cytoskeleton. *Biophysical reviews* **2018**, *10*, 1587−1604.
(81) Chiaruttini, N.; Redondo-Morata, L.; Colom, A.; Humbert, F.; Lenz, M.; Scheuring, S.; Roux, A. Relaxation of Loaded ESCRT-III Spiral Springs Drives Membrane Deformation. *Cell* **2015**, *163*, 866−879.
(82) Lu, Y.; Liu, J. Functional DNA nanotechnology: emerging applications of DNAzymes and aptamers. *Curr. Opin. Biotechnol.* **2006**, *17*, 580−588.
(83) Fabrini, G.; Minard, A.; Brady, R. A.; Di Antonio, M.; Di Michele, L. Cation-Responsive and Photocleavable Hydrogels from Noncanonical Amphiphilic DNA Nanostructures. *Nano Lett.* **2022**, *22*, 602−611.
(84) Del Grosso, E.; Ragazzon, G.; Prins, L. J.; Ricci, F. Back Cover: Fuel-Responsive Allosteric DNA-Based Aptamers for the Transient Release of ATP and Cocaine (Angew. Chem. Int. Ed. 17/2019). *Angew. Chem., Int. Ed.* **2019**, *58*, 5772.
(85) Hernández-Ainsa, S.; Ricci, M.; Hilton, L.; Aviñó, A.; Eritja, R.; Keyser, U. F. Controlling the Reversible Assembly of Liposomes through a Multistimuli Responsive Anchored DNA. *Nano Lett.* **2016**, *16*, 4462−4466.

https://doi.org/10.1021/jacs.3c01493
J. Am. Chem. Soc. 2023, 145, 11265−11275